Highly oriented and fully dense CGO films prepared by spray-pyrolysis and different precursor salts

L. dos Santos-Gómez[a], J. Zamudio-García[a], J.M. Porras-Vázquez[a], E.R. Losilla[a], D. Marrero-López[b,*]

[a]Universidad de Málaga, Departamento de Química Inorgánica, 29071-Málaga, Spain.
[b]Universidad de Málaga, Departamento de Física Aplicada I, 29071-Málaga, Spain.

ABSTRACT

CeO_2–based thin films are prepared by spray-pyrolysis deposition from different aqueous precursor solutions containing nitrate, chloride or acetate salts. The morphology and orientation growth strongly depends on the precursor type. Acetate solutions lead to dense films with improved microstructural features, i.e. uniform film thickness and a low roughness of 1.5 nm. Films with different Gd-content ($Ce_{1-x}Gd_xO_{2-x/2}$, $0 \leq x \leq 0.2$, CGO) are prepared from acetate salts. These films show a (200) preferred orientation growth, regardless of the substrate type, i.e. fused quartz and polycrystalline ceramics. The in-plane conductivity of the films on quartz is lower than that of the bulk material, possibly due to the different thermal mismatch between the substrate and the film. These CGO films are also evaluated as protective layers to prevent the reaction between the $Zr_{0.84}Y_{0.16}O_{1.92}$ (YSZ) electrolyte and the $La_{0.6}Sr_{0.4}Co_{0.2}Fe_{0.8}O_{3-\delta}$ (LSCF) cathode. The electrode efficiency of LCSF improves greatly after the introduction of a 150 nm thin CGO interlayer.

Keywords: CeO_2; thin film; spray-pyrolysis; Solid Oxide Fuel Cells

* Corresponding author.
E-mail address: marrero@uma.es (David Marrero-López)
Present address: Dpto. de Física Aplicada I, Facultad de Ciencias, Campus de Teatinos, Universidad de Málaga, 29071-Málaga, Spain.
Tel: +34 952137057, Fax: +34 952132382

1. Introduction

Doped-cerium oxide thin films have numerous electrochemical applications, including electrolytes for solid oxide cells (SOCs), gas sensors and diffusion barrier layers [1-4]. In particular, a layer of CGO is widely used to prevent reaction between the $Zr_{0.84}Y_{0.16}O_{1.92}$ (YSZ) electrolyte and the $La_{0.6}Sr_{0.4}Co_{0.2}Fe_{0.8}O_{3-\delta}$ (LSCF) cathode in a fuel cell [5-8]. These films need to be sufficiently thin and dense to avoid additional ohmic losses in the electrochemical devices. Screen-printing is the most commonly used method to prepare CeO_2-based interlayers with thickness of several microns; however, sintering temperatures up to 1400 ºC are needed to obtain dense layers. Such high temperatures lead to reactivity between YSZ and CGO at only 1100 ºC [9]. Recent studies have also reported that a porous CGO interlayer is not effective as protective layer because alkaline-earth elements, such as Sr^{2+}, easily diffuse on the porous surface of the CGO grains and react with YSZ [10-11]. Hence, dense CGO films and low-temperature fabrication methods are required to minimize the possible reactivity between the materials. In addition, the finer grains, obtained at low fabrication temperatures, contribute toward improving the thermomechanical performance.

Different physical methods, such as pulsed laser deposition and magnetron sputtering, have been employed to fabricate CGO films [12-20]. However, these methods are used at laboratory-scale and require rigorous synthetic conditions of temperature, gas atmosphere and oxygen partial pressure to control the cation stoichiometry of the resulting films. Thus, differences between the film and the target composition are usually reported [21,22]. Other techniques like spin-coating and dip-coating require multiple and tedious fabrication steps [23,24]. Consequently, facile, efficient, reproducible and industrially viable synthesis techniques are needed to obtain dense CGO films.

In this context, spray-pyrolysis has demonstrated to be a scalable and simple method to produce homogeneous materials, composites and functional nanostructures over large areas. In particular, this is an effective method for preparing a variety of film morphologies with a precise controlled stoichiometry. Moreover, unlike other methods, a very simple experimental setup is required, which can be easily scaled up for mass-production as a continuous fabrication technique [25-27].

In the spray-pyrolysis technique, a precursor solution is sprayed using an atomizer onto a heated substrate, obtaining dense or porous films, depending on the deposition conditions [28-30]. The precursors are commercially available and of low cost, unlike the targets for physical deposition methods. The morphology and uniformity of the films, i.e. thickness, porosity, grain size, can be easily tailored by varying the deposition parameters, such as temperature, time and post-thermal treatments [31,32]. It is also evident that the morphology of the films depends on the properties of the precursor solutions. Different salts have different solute precipitation and decomposition processes, leading to different microstructures.

In the present work, CGO films are prepared by spray-pyrolysis deposition by employing different aqueous precursor solutions, i.e. nitrate, acetate and chloride salts, under the same synthetic conditions. The structural and microstructural features are investigated by different techniques. The films obtained from acetate precursors, with better quality, were further characterized and their potential application as protective layer was evaluated by impedance spectroscopy in a symmetrical LSCF/YSZ/LSCF cell.

2. Experimental

2.1. Materials preparation.

Films with different Gd-content were prepared: $Ce_{1-x}Gd_xO_{2-x/2}$ (x=0, 0.05, 0.1 and 0.2). For simplicity reasons, the composition of the samples is hereafter denoted as CGOx, where x represents the Gd-content in mol.%. The films were deposited by chemical spray-pyrolysis on different substrates: fused silica (quartz of 5×3 cm^2) and polished surface pellets of $Zr_{0.84}Y_{0.16}O_{1.92}$ and $La_{0.9}Sr_{0.1}Ga_{0.8}Mg_{0.2}O_{1.85}$ (LSGM). The YSZ and LSGM pellets were prepared from commercial powders supplied by Tosoh and freeze-dried precursors, respectively [33]. The powders were compacted into disks of 10-25 and 1 mm of diameter and thickness, respectively, and sintered in air at 1400 ºC for 4 h. Then, the pellet surfaces were polished with diamond paste down to 1 μm before the spray-pyrolysis deposition.

Different metal salts were used as starting precursors: nitrates ($Ln(NO_3)_3 \cdot 6H_2O$, 99.99%), acetates ($C_6H_9LnO_6 \cdot H_2O$, 99.9%) and chlorides ($LnCl_3 \cdot 7H_2O$, 99.9%), Ln=Ce, Gd, all of them supplied by Sigma-Aldrich. In general, low boiling point solvents, such as ethylene-glycol and ethanol are usually used in the literature; however, in the present study, no toxic aqueous solutions were used by considering the possible industrial application. The precursor solutions were prepared by dissolving the salts in deionized water under constant stirring to obtain transparent solutions with a final concentration of 0.02 mol L^{-1}. The hydration water of the salts was firstly verified by thermogravimetric analysis in air. In the case of the films prepared from metal nitrates, citric acid was used as chemical additive, with citric-acid/metal ratio between 0.125 and 0.5, to improve the adherence to the substrates as discussed below. The wettability properties of these solutions were investigated by contact angle measurements (KSV CAM 101).

The spray-pyrolysis equipment was described in details earlier [29]. The substrates were heated on an aluminium block at a constant temperature of 450 ºC. The precursor solutions were fed to the spray nozzle with a liquid flow rate of 20 $mL \cdot h^{-1}$ and atomized with air at a pressure of approximately 2 bar. The nozzle-to-substrate distance was fixed at 20 cm and the deposition time was varied between 5 and 30 min. After the deposition, the films were treated in a furnace in air atmosphere between 650 and 1000 ºC for 2 h to investigate the phase and microstructural evolution with the temperature. A low heating/cooling rate of 2 ºC min^{-1} was used during all thermal treatments to minimize the thermal stress associated with the thermal expansion mismatch between the film and quartz substrates.

2.2. Structural and microstructural characterization.

X-ray powder diffraction (XRD) was performed with a Empyrean PANalytical diffractometer and $CuK_{\alpha 1,2}$ radiation. The patterns were analyzed with the GSAS suite software [34].

The morphology of the films was explored by scanning electron microscopy (FEI-SEM, Helios Nanolab 650), equipped with a Tomahawk focused ion beam (FIB); atomic force microscopy (AFM) with a MultiMode V (Veeco); and transmission electron microscope (FEI-TEM Talos F200X). For TEM observation, electron-transparent lamellas were prepared by using the procedure described elsewhere [35]. The composition of the films was checked by X-ray dispersive spectroscopy (X-Max Oxford instrument). The grain size

distribution was determined via the linear interception method with the help of Estereologia software from both SEM and AFM micrographs [36].

2.3. Electrical characterization.

The electrical properties of the films were investigated by impedance spectroscopy using a Solartron 1260 FRA in a 2-probe configuration. The in-plane conductivity was determined for films deposited on insulating quartz (0.5×0.5 cm^2). For this purpose, two parallel electrodes were deposited by coating Pt-ink on the film surface and Pt wires were attached and connected to the impedance analyzer. The impedance spectra of the blank quartz were also acquired to confirm a negligible influence of the substrate on the electrical conductivity of the films.

The CGO films were also investigated as a protective interlayer to prevent the reaction between the $La_{0.6}Sr_{0.4}Co_{0.2}Fe_{0.8}O_{3-\delta}$ (LSCF) cathode and the YSZ electrolyte. Symmetrical cells of LSCF/YSZ/LSCF without and with a CGO interlayer were prepared from LSCF powders obtained from freeze-drying precursors. The LSCF powders have an average particle size of 100 nm after sintering at 900 ºC for 1 h [37]. The LSCF powders were mixed with Decoflux™ to obtain and ink, which was deposited symmetrically onto the YSZ pellets by screen-printing and then sintering at 1100 ºC for 2 h. Before the LSCF deposition, the CGO films were treated at 800 ºC for 1 h. The polarization resistance of the symmetrical cells was determined by impedance spectroscopy. The data were collected in air on cooling between 800 and 400 ºC, with a dwell time of 30 min at each measured temperature. The stability of the cells was investigated at 700 ºC for 150 h and both serial and polarization resistance were determined as a function of time. An ac-voltage amplitude of 300 and 50 mV was used for the in-plane conductivity and polarization resistance measurements, respectively, and the frequency was varied between 10 mHz and 1 MHz. The data were processed with the Zview software [38].

3. Results and Discussion

3.1. CeO_2 films prepared from different precursors.

Undoped CeO_2 films were firstly prepared on amorphous quartz substrates, under the same synthetic conditions for the different precursors, to better study the structural characteristics. The deposition temperature was 450 ºC to ensure complete thermal decomposition of the precursors and to minimize the presence of residual solvents and organic residues, which may lead to the formation of cracked and porous films after the subsequent thermal treatment in a furnace [28]. In general, if the deposition temperature is much higher than the precursor decomposition temperature, the salts partially decompose in the still-liquid phase. Thus, the tensile stress during the decomposition is reduced and crack free films are obtained [42].

According to previous studies, the thermal decomposition of the precursors takes place in the temperature range of 280 - 460 ºC. The decomposition of cerium nitrate occurs in two consecutive steps below 300 ºC, whiles cerium chloride decomposes completely above 280 ºC in only one thermal process [39-41]. On the other hand, cerium acetate shows a more complex decomposition process with the formation of multiple

phases below 460 ºC [41]. The different decomposition of these salts affects the film morphology as discussed below.

Fig. 1 compares the XRD patterns of the as-prepared CeO_2 films from the different precursors. As can be observed, they are crystalline at 450 ºC with preferred growth orientation along the (111) for nitrates and along the (200) plane for chloride and acetate salts. The average crystallite size, estimated by the Scherrer´s equation, after correction for instrumental line broadening using a LaB_6 standard material, takes values of ~12 nm for samples prepared from nitrate and chloride salts, and ~8 nm for acetates. The smaller crystal size of the films prepared from acetate precursors is possibly related to the highest decomposition temperature.

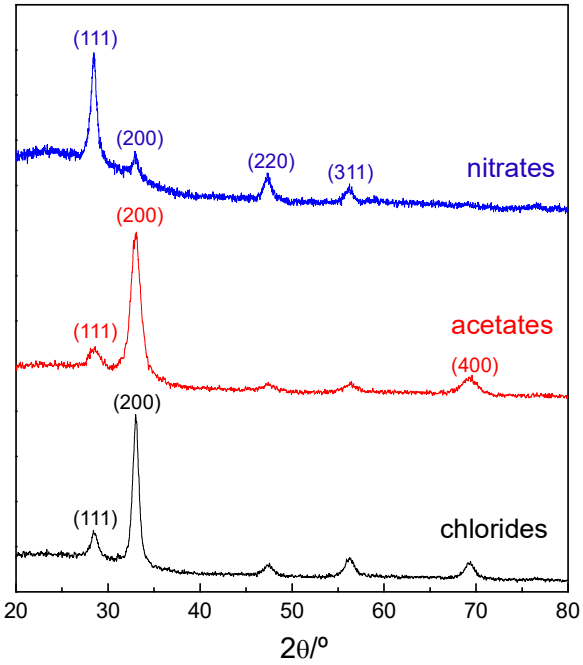

Fig. 1. XRD patterns of as-prepared CeO_2 films obtained from different precursor salts and deposited on quartz at 450 ºC for 10 min.

TEM images confirm that the films at 450 ºC are highly crystalline and formed by nanocrystals of 5-10 nm of diameter, similar to that estimated by the Scherrer´s equation (Fig. S1, supplementary information).

All the films display good adherence to the substrate, regardless the precursor salt employed. In addition, they are optically transparent and homogenous over an area of 5×3 cm^2, especially those obtained from acetate salts.

SEM images of the as-deposited films at low magnification are displayed in Fig. 2. The acetate films are strongly adhered to the substrate with a very uniform and smooth surface, comprised of regular circular deposits from the individual droplets, which form the film upon deposition (Fig. 2a). According to Muecke *et al.* this disc type of morphology is the most desired as the area under each deposit is completely covered by the metal salt and only few layers of deposits are required to obtain a continuous coating [42].

The film obtained from nitrates shows a more irregular deposit, which is related to the formation of bubbles in the droplet from salt decomposition during evaporation, which results in the distortion of the circular deposits (Fig. 2b). A similar behavior was observed in NiO-CGO films prepared from nitrate precursors [42]. In addition, small hollow spheres with diameters between 1 and 5 μm are observed on the surface, attributed

to precursor precipitation within droplets before impacting the substrate as a consequence of the low decomposition temperature of nitrate salts. The amount of spheres, which are not desired because they contribute to the film roughness and porosity, increases gradually with the concentration of citric acid (Fig. S2). As it was commented in the experimental section, citric acid is used as chemical additive to improve the adherence of the film to the substrate. Films obtained from only nitrates showed poor adherence at deposition temperatures between 300 and 450 ºC. Furthermore, pinholes are observed for films with low citric acid content (Fig. S2a). The addition of citric acid improves wettability, thus the contact angle decreases from 70º to 50º for solutions without and with citric acid (L/M=0.25), respectively.

Finally, chloride precursors lead to a rough film surface morphology with the presence of cracks (Fig. 2c). Hence, under the synthetic conditions used, cerium acetates lead to films with improved microstructural features, i.e. low surface roughness and crack free. As a consequence, only $Ce_{1-x}Gd_xO_{2-x/2}$ films prepared from acetate salts are further investigated in the present work.

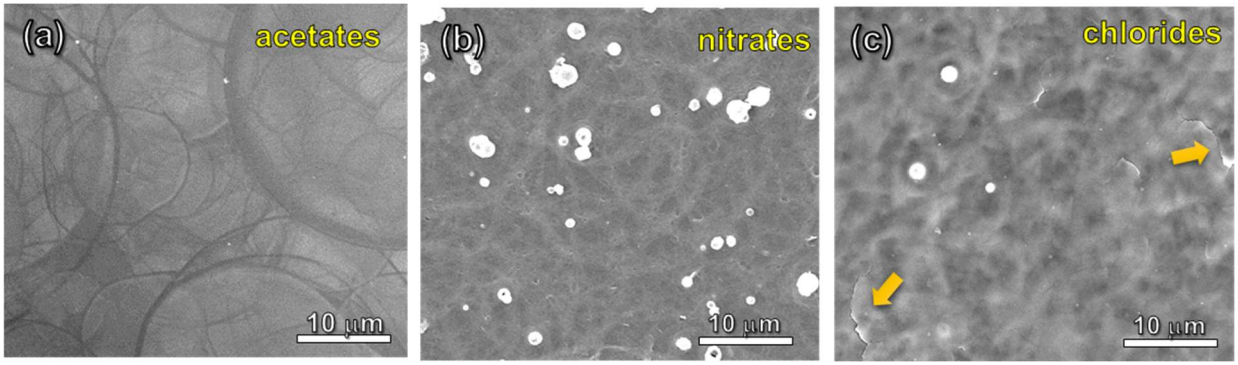

Fig. 2. SEM image of as-prepared CeO_2 films obtained from different precursor salts and deposited on quartz at 450 ºC for 5 min.

3.2. $Ce_{1-x}Gd_xO_{2-\delta}$ films prepared from acetate precursors.

XRD patterns of CGO films prepared from acetate precursors on quartz are shown in Fig. 3a. All films are highly oriented along the [100] direction, thus only two diffraction peaks assigned to (200) and (400) Bragg planes are observed in the 2θ range of 20-80º. The same films were deposited on polycrystalline ceramic pellets of YSZ under similar spray conditions, and the same preferred crystallographic growth was found (Fig. 3b). Moreover, this is independent on the deposition time (5-30 min) and annealing temperature (Fig. S3). Similar results were obtained for CGO films deposited on LSGM pellets, although they are not included in the manuscript, suggesting that the preferred oriented growth is independent on the substrate type.

XRD patterns were analyzed by the Rietveld method in the $Fm\bar{3}m$ space group, taking into account the preferred orientation along the [100] direction (Fig. 3c). During the Rietveld analysis, only the cell parameters, scale factor, background, zero shift and peak symmetry parameters were refined. The corresponding unit cell volume of the films deposited on quartz and YSZ pellets are similar, following a linear dependence on Gd-doping (Fig. 3d). This clearly indicates the formation of a solid solution in the whole compositional range studied $0 \leq x \leq 0.2$, therefore, dopant segregation is expected to be negligible.

TEM images for CGO10 show a dense layer formed by particles of approximately 20 nm of diameter without the presence of amorphous or phase segregations (Fig. 3e). Fig. 3f shows the HRTEM image where

three grains and grain boundaries meet, and the corresponding Fast Fourier Transform (FFT) patterns. The grain boundary is free of impurities and the particles have a preferred orientation growth along the [100] crystallographic direction.

Surface and cross-sectional morphology of the different films on YSZ are shown in Fig. 4. The thickness of the layers is similar for the different compositions, ranging from 350 to 400 nm after 15 min of spray deposition (Table 1). A nearly linear relationship exists between the film thickness and deposition time (Fig. S4). Thus, the films thickness can be easily tailored from 150 to 800 nm by varying the deposition time between 5 and 30 min. It is also worth noting that uniform film thicknesses are obtained for deposition times as short as 5 min (Fig. S4).

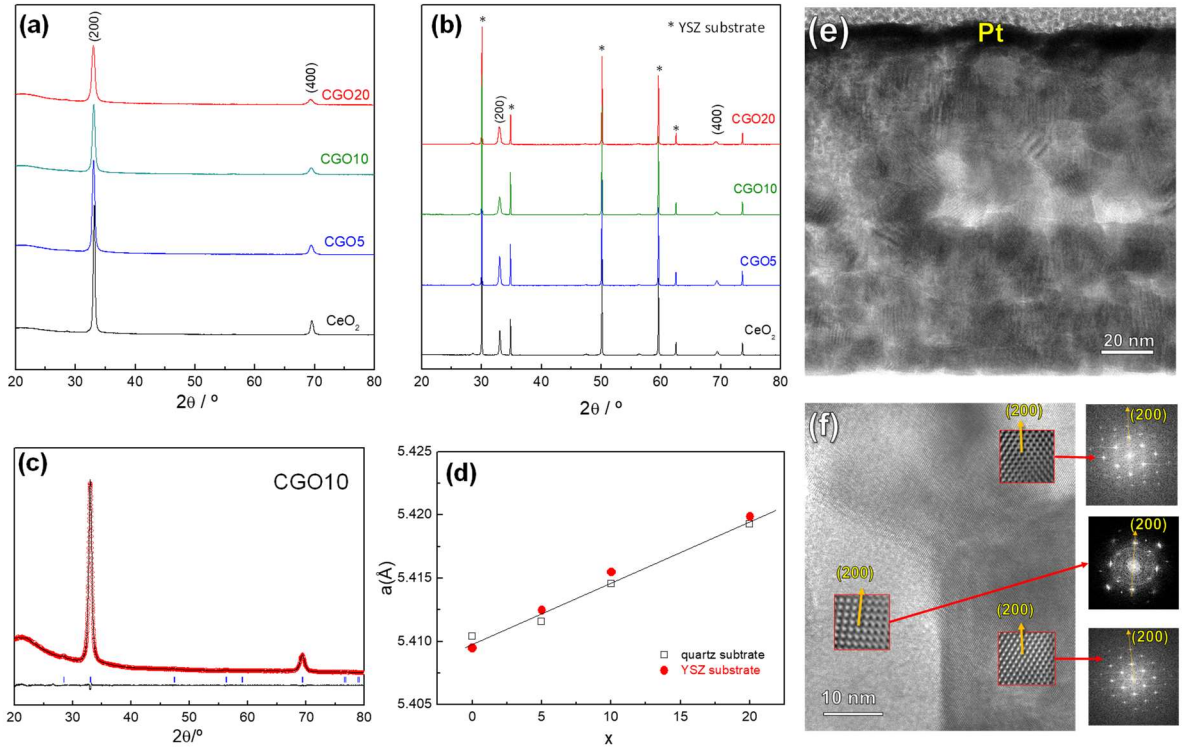

Fig. 3. (a) XRD patterns of $Ce_{1-x}Gd_xO_{2-x/2}$ (x=0-0.2), prepared from acetate salts, deposited on (a) quartz and (b) polished YSZ pellets and calcined at 800 ºC for 2 h. (c) Representative Rietveld plot of CGO10. (d) Variation of the unit cell parameter as a function of the Gd-content for films prepared on quartz and YSZ. (e) TEM image of CGO10 on YSZ, and (f) HRTEM image and the corresponding FFT.

Table 1. SEM-EDS analysis of $Ce_{1-x}Gd_xO_{2-\delta}$ (x=0-0.2) thin films on YSZ from acetate precursors.

T(ºC)	Sample	Ce (atm.%)	Gd (atm. %)	d(nm)^{SEM}	Thickness (nm)	Rms (nm)
800	x=0	100	--	52.7	400	1.94
	x=0.05	94.70(1.26)	5.30	52.0	380	1.88
	x=0.1	89.89(0.86)	10.11	40.9	350	1.28
	x=0.2	81.34(1.22)	18.66	26	420	1.58
1000	x=0	100	--	84.5	--	--
	x=0.05	95.08(0.95)	4.92	65.1	--	2.92
	x=0.1	90.13(1.60)	9.87	52	--	--
	x=0.2	81.43(1.13)	18.57	33.6	--	--

*Standard deviations based on four independent measurements are shown in brackets. Root mean square roughness (Rms).

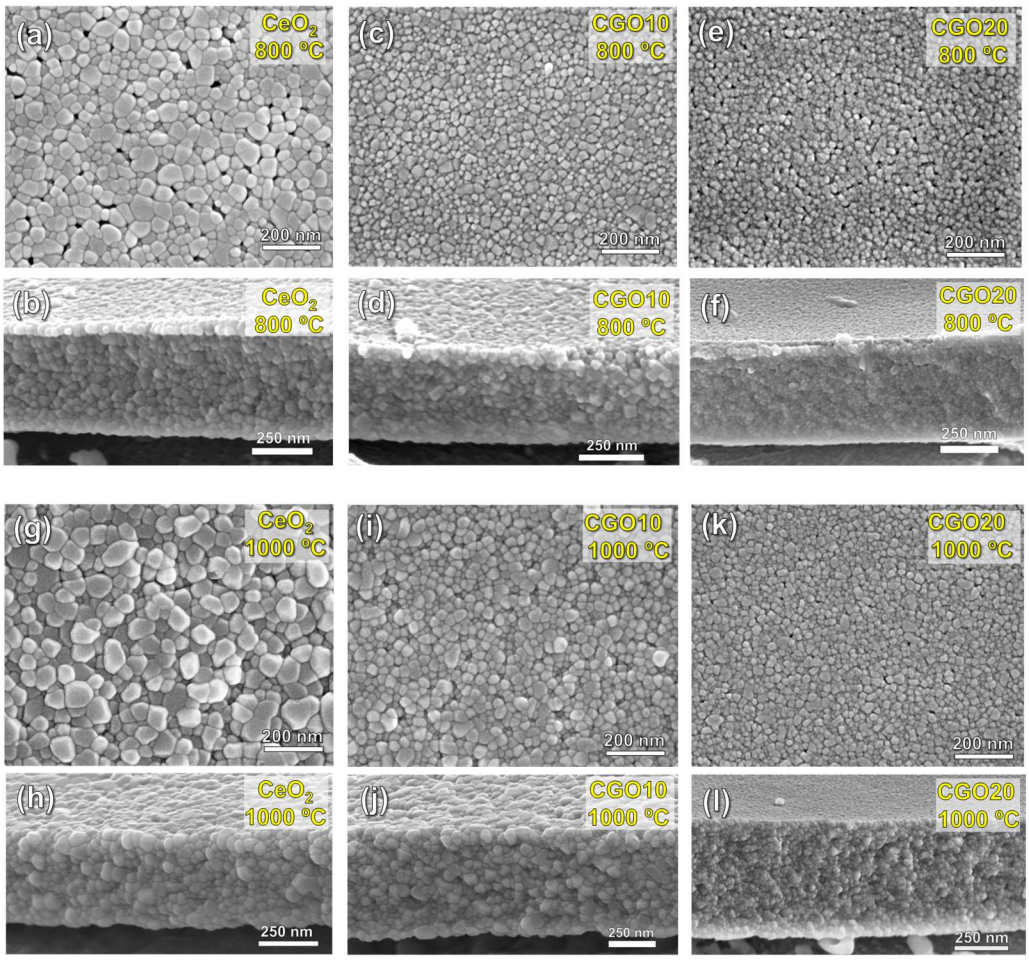

Fig. 4. Surface morphology and cross-section SEM images of CGO films on YSZ prepared from acetate salts and sintered at (a-f) 800 and (g-l) 1000 ºC for 2 h.

Cross-sectional SEM images reveal that the films are dense with certain superficial porosity for samples treated at 800 ºC for 2 h (Fig. 4a-f); however, the films become completely dense after sintering at 1000 ºC (Fig. 4g). The most remarkable difference between the film morphologies is the average grain size, which depends on Gd-doping. The grain size of all films treated at 800 ºC decreases with Gd-content from 53 nm for CeO_2 to 28 nm for CGO20. The same films treated at 1000 ºC exhibit a large grain size, i.e. 84.5 and 33.6 nm for CeO_2 and CGO20, respectively. Similar observations were reported previously for thin films and pellets of doped-CeO_2 [43,44].

The reduction of the grain size with doping is usually attributed to different factors, including the nature of the initial precursors, lattice distortion after doping, microstrains, and grain boundary dopant segregation [45]. The nature of the precursors and the amount of defects introduced during the preparation method affect the grain growth. Thus, the introduction of defects may act similarly like dopants, resulting in a lower grain growth. The difference in the sizes of Gd^{3+} and Ce^{4+} causes a local distortion in the crystal lattice and the defect interaction aggregation reduce the mobility of cations at the grain boundary, lowering grain growth rate. On the other hand, Gd^{3+} exhibits an effective negative charge compared to Ce^{4+} and this tends to enrich at grain boundary due to space charge phenomena [44]. This generates a concentration gradient that retains the cation diffusion along the grain boundary, hindering the grain growth.

The cation composition and homogeneity of the films was evaluated by EDX analysis. Table 1 compares the cation stoichiometry of the films, which is similar to the nominal one, taking into account the experimental error of this technique. The EDX mapping further confirms a homogeneous distribution of elements in the whole film thickness (Fig. S5).

The superficial morphology of the films on quartz was further analyzed by AFM in a 0.5×0.5 μm^2 area. A continuous surface with rounded grains and low porosity is observed (Fig. 5). The films exhibit a low root mean square roughness, which decreases slightly with Gd-doping from 1.94 nm for pure CeO_2 to 1.58 nm for CGO20. This behavior is attributed to a finer grain size with increasing Gd-doping. On the other hand, the average grain size, determined from the AFM image, is comparable to that obtained from SEM (Fig. S6 and S7). The grain size of CGO10 grows from 38.6 to 52.0 nm after sintering at 800 and 1000 ºC, respectively, which is also accompanied by an increase of the roughness from 1.28 to 2.92 nm (Fig. S8). It is worth noting that the values of roughness are rather low when compared to those reported in the literature [46-55]. Table S1 compares the roughness of CeO_2 – based films obtained by different fabrication methods, which vary between 1.6 and 500 nm.

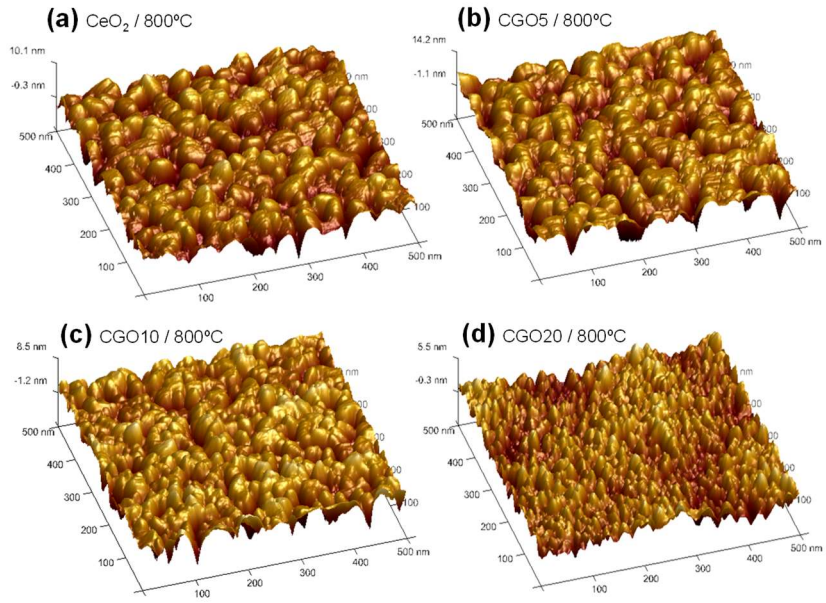

Fig. 5. 3D AFM image of CGO films on quartz prepared from acetate precursors and calcined at 800 ºC for 2 h.

3.3. Electrical properties.

The inset of Fig. 6 shows a representative impedance spectrum for CGO10 film deposited on quartz and measured at 500 ºC in an in-plane configuration. The films were prepared by spray-pyrolysis at 450 ºC for 15 min and then treated at 800 ºC for 2 h in air.

The spectra are apparently composed of two overlapped processes, which are not adequately separated by equivalent circuit fitting because the intermediate frequency arc at 10 kHz dominates the spectra, and the high frequency contribution at 1 MHz is only observed at low temperatures (inset Fig. 6). Since the measurements were performed in an in-plane configuration, the resistance of the films is very high due to its large geometric factor $L/S=5\cdot10^4$ cm^{-1}, where L is the distance between the electrodes and S the cross-sectional area of the film. For this reason, spectra are not acquired at temperatures lower than 450 ºC.

The capacitance of two processes are of the order of 5 10^{-12} F cm^{-1}, instead of the typical 10^{-12} F cm^{-1} and 10^{-9} F cm^{-1} for the bulk and grain boundary response, respectively. The theoretical capacitances of the bulk, C_b, and grain-boundary, C_{gb}, processes can be estimated by assuming the classical brick-layer model [56,57]:

$$C_b = \varepsilon_o \varepsilon_r \frac{A}{L} \qquad (1)$$

$$C_{gb} = \varepsilon_o \varepsilon_r \frac{A}{L} \frac{d_g}{\delta_{gb}} \qquad (2)$$

where ε_o and ε_r~25 are the vacuum and dielectric constant of CGO, respectively, and d_g and δ_{gb}~1 nm are the average grain size and grain-boundary thickness, respectively [58,59]. From Eqs 1 and 2, the theoretical capacitance of bulk and grain-boundary processes are of the order of 10^{-16} and 10^{-15} F cm^{-1}, respectively, much lower than the parasitic capacitance introduced by the equipment ~pF. Thus, the arcs observed in the spectra may not be affirmatively assigned to bulk or grain boundary conduction.

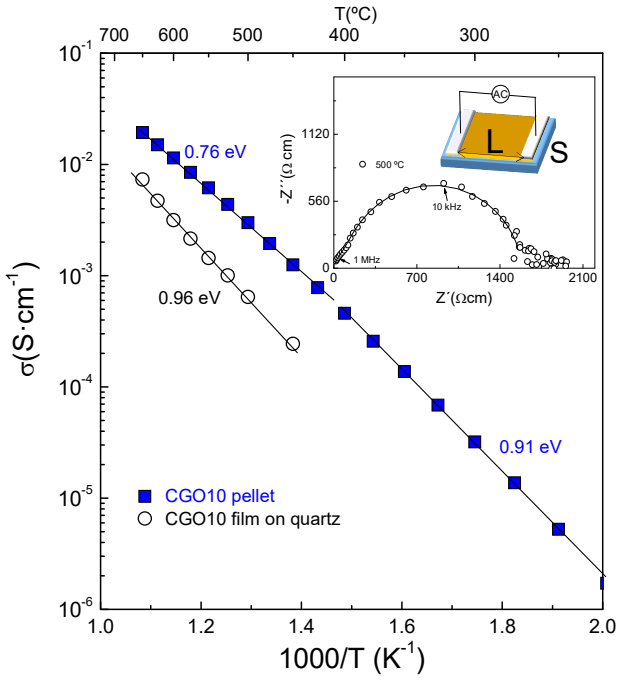

Fig. 6. Temperature dependence of the in-plane conductivity of CGO10 film on quartz and pellet. The inset figure shows the impedance spectra of CGO10 film.

Fig. 6 compares the in-plane conductivity of a CGO10 film and a polycrystalline pellet with the same composition but micrometric grain size. As can be observed, the conductivity of the film is lower than that of the pellet, i.e. 3 and 11 mS cm^{-1} for the film and pellet, respectively, at 600 ºC. The lower values of conductivity of the film may be attributed to the lattice strain induced by the different thermal expansion coefficients between the film and the substrate materials [60]. In addition, high microstrain was observed previously in CGO films prepared by spray-pyrolysis, affecting negatively to the transport properties. According to Rupp *et al.*, the microstrain decreases with the increase of temperature and annealing time [45].

The conductivity values of CeO_2-based films, reported in the literature, vary in a broad range, depending on the fabrication method, substrate, annealing temperature and microstructure. Table S1 compares

these data for previous works, and the conductivity varies from 0.1 to 12 mS cm^{-1} at 600 ºC [46-55]. The highest values are found for CeO_2 deposited by spray-pyrolysis at 500 ºC on glass, e.g. 5.9 mS cm^{-1} at 350 ºC. In the present study, CGO films were also prepared on glass at 450 ºC, and the conductivity was one order of magnitude superior to that ascribed to the bulk material. This surprising increase of the conductivity was attributed to Na-conduction because sodium migrates from the glass substrate to the CGO film, as confirmed by SEM analysis. As a consequence, these data are not included in this work.

It is also evident that the film conductivity is affected by the nanometric grain size as the number of grain boundary interfaces increases. The Arrhenius plot of the total conductivity for the pellet shows two different regimes at low and high temperature with activation energies of 0.91 and 0.76 eV, respectively. The lower activation energy at high temperature is mainly associated with a minor contribution of the grain boundary resistance as well as a lower concentration of vacant-dopant defects. In contrast, the films show a higher activation energy of 0.96 eV in the whole temperature range, suggesting that the total conductivity is seriously affected by the grain-boundary process.

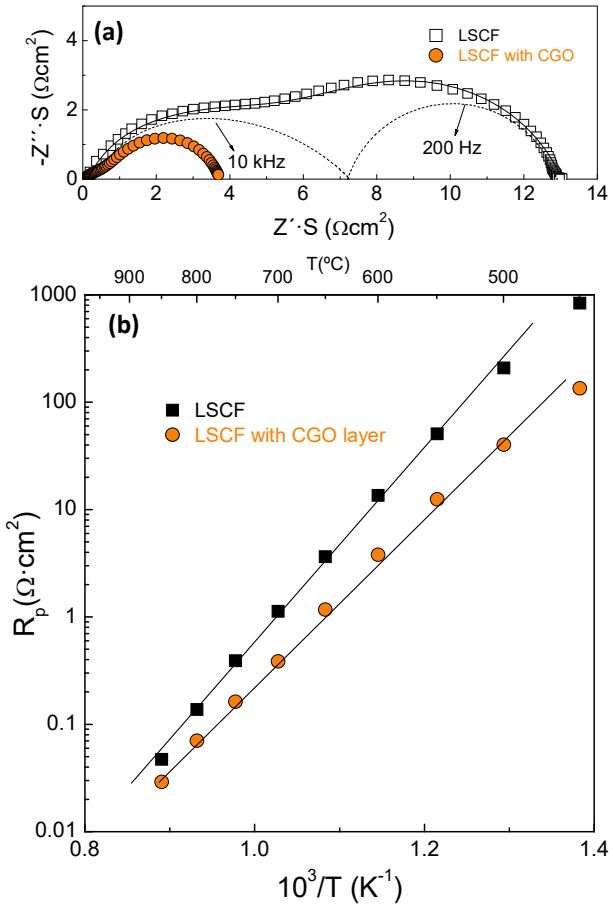

Fig. 7. (a) Impedance spectra of LSCF without and with CGO10 interlayer at 600 ºC. (b) Temperature dependence of the polarization resistance.

In order to evaluate the potential application of the CGO films as protective layer, LSCF/YSZ/LSCF symmetrical cells without and with CGO interlayers are investigated. The impedance spectra confirm that the introduction of CGO interlayers produces a significant reduction of the polarization resistance of LSCF in

contact with YSZ, from 13.5 to 4 Ω cm^2 at 600 ºC (Fig. 7a). Two different contributions are distinguished in the impedance spectra, which are simulated by using an equivalent circuit $R_s(RQ)_1(RQ)_2$, where R_s is the ohmic resistance of the cell and two (RQ) elements associated with the electrode polarization contribution (Fig. 7c). The high frequency arc, with a relaxation frequency of ~10 kHz and an associated capacitance of about 0.05 $mFcm^{-2}$, is usually assigned to the charge transfer process at the electrode/electrolyte interface, while the low frequency contribution at ~200 Hz has a higher capacitance, ~1 $mFcm^{-2}$, and is attributed to the dissociation/adsorption of oxygen molecules on the electrode surface [61,62].

The high frequency contribution, related to the charge transfer, is more important for the cell without a protective CGO layer. This phenomenon is usually associated with the formation of $SrZrO_3$ at the electrode/electrolyte interface during the sintering process, which deteriorates the electrode performance due to oxide ion blocking effects. Thus, the lower polarization resistance of the cell with a CGO interlayer is attributed to the combination of two different factors: the inhibition of the formation of $SrZrO_3$, and to an improvement of the oxygen incorporation at the cathode/electrolyte interface as a consequence of the higher ionic conductivity of CGO compared to YSZ.

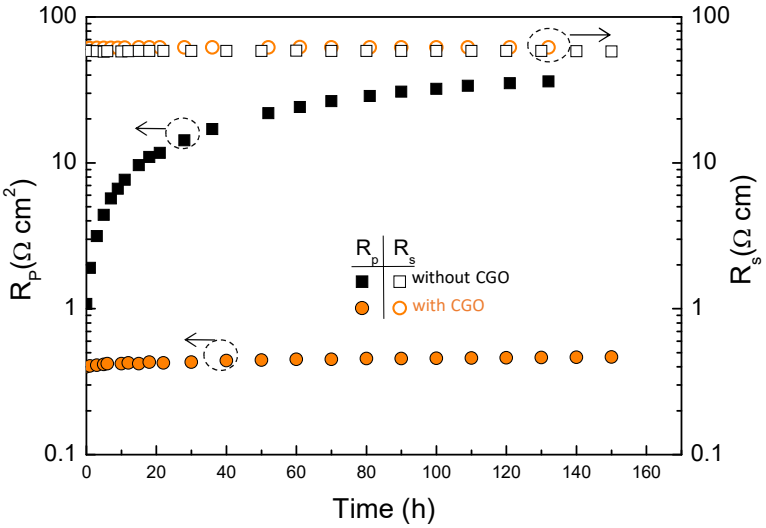

Fig. 8. Variation of the polarization (R_p) and ohmic resistance of the LSCF/YSZ/LSCF symmetrical cells without and with CGO10 protective layer.

It is well reported in the literature that the interfacial formation of $SrZrO_3$ in the LSCF-YSZ system depends on the fabrication method and optimization of the sintering temperature of both LSCF and CGO layers [63-65]. In a previous work, we demonstrated that dense CGO layer, obtained by spray-pyrolysis, are only effective to suppress Sr diffusion at temperatures lower than 800 ºC [9]. At high temperatures, Sr species from LSCF easily diffuse on the porous surface of the CGO grains and react with YSZ [9,10]. For this reason, the long-term stability of the cell was investigated at 700 ºC. The polarization resistance of the cell without protective layer suffer a strong degradation over time, increasing continuously from 1 to 36 Ω cm^2. However, the ohmic resistance of the symmetrical cells, which is predominantly associated with the thick electrolyte, is less affected, varying from to 58 to 58.5 Ωcm. This confirms that the degradation is mainly due to changes at

the electrolyte/cathode interface. The SEM/EDX image demonstrate the formation of a Sr-rich layer, attributed to $SrZrO_3$, with a thickness of approximately 1 μm (Fig. S9 a).

In the case of cell with CGO protective layer, the variation of both polarization and ohmic resistance are rather low, e.g. R_p varies from 0.4 to 0.45 Ω cm^2, possibly due to minor microstructural changes of the electrodes, such as particle growth and coarsening and possibly Sr-surface degradation as previously reported for these compounds at intermediate temperatures [62,65]. The SEM analysis does not significant Sr and Zr diffusion though the CGO interlayer (Fig. S9 b). Hence, CGO thin films, prepared by spray-pyrolysis deposition, are effective protective layers at least at low operating temperature.

CONCLUSIONS

CGO thin films were prepared by spray-pyrolysis deposition and different precursor salts. The films were crystalline and showed a preferred crystallographic orientation along the (110) plane for nitrates and the (200) plane for chloride and acetates, regardless of the substrate used, i.e. fused quartz and polycrystalline ceramic pellets. The film morphology strongly depended on the precursor type. Films obtained from acetates showed a very low roughness, about 1.5 nm, and uniform thickness over large areas, which is competitive with different preparation methods previously reported. The average grain size, determined from both SEM and AFM images, decreased with increasing Gd-doping from 53 nm for pure CeO_2 to 28 nm for CGO20 at 800 ºC due to space charge effects. Thin and continuous CGO films of 150 nm of thickness were obtained for short deposition times of only 5 min, which is interesting for industrial application. The film thickness was tailored from 150 to 800 nm in only one step by varying the deposition time from 5 to 30 min.

The in-plane conductivity, about 3 mS cm^{-1} at 600 ºC, was negatively affected by the lattice strain due to thermal mismatch between the films and quartz substrate, and possible microstrains due to the low firing temperature and short sintering time.

Symmetrical LSCF/YSZ/LSCF without a CGO interlayer suffer a strong degradation of the polarization resistance over time, increasing from 1 to 36 Ωcm^2 at 700 ºC for 140 h. In contrast, the introduction of a thin CGO interlayer is effective to prevent the reactivity at the LSCF/YSZ interface, and to improve the electrode performance at low operating temperature.

ACKNOWLEDGEMENTS

This work was supported by MINECO through the RTI2018-093735-B-I00 and UMA18-FEDERJA-033 research grants (Spain), which are co-funded by FEDER. J.Z-G thanks to the Spanish Ministry of Education, Culture and Sport for his FPU grant (FPU17/02621). J.M.P-V. thanks the University of Málaga for the funding.

REFERENCES

[1] J. Leng, Z. Wang, J. Wang, H.H. Wu, G. Yan, X. Li, H. Guo, Y. Liu, Q. Zhang, Z. Guo, Advances in nanostructures fabricated via spray pyrolysis and their applications in energy storage and conversion, Chem. Soc. Rev. 48 (2019) 3015-3072.

[2] Y. Kosto, A. Zanut, S. Franchi, Y. Yakovlev, I. Khalakhan, V. Matolín, K.C. Prince, G. Valenti, F. Paolucci, N. Tsud, Electrochemical activity of the polycrystalline cerium oxide films for hydrogen peroxide detection Appl. Surf. Sci. 488 (2019) 351-359.

[3] A.S. Mokrushin, E.P. Simonenko, N.P. Simonenko, K.A. Bukunov, V.G. Sevastyanov, N.T. Kuznetsov, Gas-sensing properties of nanostructured CeO_2-xZrO_2 thin films obtained by the sol-gel method, J. Alloys Compd.773 (2019) 1023-1032.

[4] L.E. Ríos-Saldaña, V.D. Compeán-García, H. Moreno-García, A.G. Rodríguez, Improvement of the conversion efficiency of as-deposited Bi_2S_3/PbS solar cells using a CeO_2 buffer layer, Thin Solid Films 670 (2019) 93-98.

[5] S.J. Kim, G.M. Choi, Stability of LSCF electrode with GDC interlayer in YSZ-based solid oxide electrolysis cell, Solid State Ionics 262 (2014) 303-306.

[6] J. Railsback, S.H. Choi, S.A. Barnett, Effectiveness of dense Gd-doped ceria barrier layers for (La,Sr)(Co,Fe)O_3 cathodes on Yttria-stabilized zirconia electrolytes, Solid State Ionics 335 (2019) 74-81.

[7] V. Wilde, H. Störmer, J. Szász, F. Wankmüller, E. Ivers-Tiffée, D. Gerthsen, $Gd_{0.2}Ce_{0.8}O_2$ Diffusion barrier layer between $(La_{0.58}Sr_{0.4})(Co_{0.2}Fe_{0.8})O_{3-\delta}$ Cathode and $Y_{0.16}Zr_{0.84}O_2$ electrolyte for Solid Oxide Fuel Cells: Effect of barrier layer sintering temperature on microstructure, ACS Appl. Energy Mater. 1 (2018) 6790-6800.

[8] P. Coddet, J. Vulliet, C. Richard, A. Caillard, A.L. Thomann, Characteristics and properties of a magnetron sputtered gadolinia-doped ceria barrier layer for solid oxide electrochemical cells, Surf. Coat. Tech. 339 (2018) 57-64.

[9] L. dos Santos-Gómez, J. Hurtado, J.M. Porras-Vázquez, E.R. Losilla, D. Marrero-López, Durability and performance of CGO barriers and LSCF cathode deposited by spray-pyrolysis, J. Eur. Ceram. Soc. 38 (2018) 3518-3526.

[10] F. Wang, M. Nishi, M.E. Brito, H. Kishimoto, K. Yamaji, H. Yokokawa, T. Horita, Sr and Zr diffusion in LSCF/10GDC/8YSZ triplets for solid oxide fuel cells (SOFCs), J. Power Sources 258 (2014) 281-289.

[11] J.C. De Vero, K. Develos-Bagarinao, H. Matsuda, H. Kishimoto, T. Ishiyama, K. Yamaji, T. Horita, H. Yokokawa, Sr and Zr transport in PLD-grown Gd-doped ceria interlayers, Solid State Ionics 314 (2018) 165-171.

[12] W. Wu, Z. Zhao, X. Zhang, Z. Liu, D. Cui, B. Tu, D. Ou, M. Cheng, Structure-designed gadolinia doped ceria interlayer for solid oxide fuel cell, Electrochem. Commun. 71 (2016) 43-47.

[13] A. Infortuna, A.S. Harvey, L.J. Gauckler, Microstructures of CGO and YSZ Thin Films by Pulsed Laser Deposition, Adv. Funct. Mater. 18 (2008) 127-135.

[14] J.G. Yu, B.C. Yang, J.W. Shin, S. Lee, S. Oh, J.H. Choi, J. Jeong, W. Noh, J. An, High growth-rate atomic layer deposition process of cerium oxide thin film for solid oxide fuel cell, Ceram. Int. 45 (2019) 3811-3815.

[15] Y.L. Kuo, S.D. Kencana, Y.M. Su, Oxygen vacancy levels on gadolinia-doped ceria interlayer deposited by atmospheric pressure plasma jet for solid oxide fuel cells, Ceram. Int. 44 (2018) 15262-15268.

[16] S. Uhlenbruck, N. Jordan, H.P. Buchkremer, V.A.C. Haanappel, D. Stöver, Thin film coating technologies of (Ce,Gd)$O_{2-\delta}$ interlayers for application in ceramic high-temperature fuel cells, Thin Solid Films 515 (2007) 4053-4060.

[17] N. Jordan, W. Assenmacher, S. Uhlenbruck, V.A.C. Haanappel, H.P. Buchkremer, D. Stöver, W. Mader, Ce0.8Gd0.2O2 - delta protecting layers manufactured by physical vapor deposition for IT-SOFC, Solid State Ion. 179 (2008) 919-923.

[18] S. Sønderby, T. Klemensø, B.H. Christensen, K.P. Almtoft, J. Lu, L.P. Nielsen, P. Eklund, Magnetron sputtered gadolinia-doped ceria diffusion barriers formetal-supported solid oxide fuel cells. J. Power Sources 267 (2014) 452.

[19] R. Knibbe, J. Hjelm, M. Menon, N. Pryds, M. Søgaard, H.J. Wang ,K. Neufeld, Cathode–Electrolyte Interfaces with CGO Barrier Layers in SOFC, J. Am. Ceram. Soc. 93 (2018) 2877-2883.

[20] M. Morales, A. Pesce, A. Slodczyk, M. Torell, P. Piccardo, D. Montinaro, A. Tarancón, A. Morata Enhanced Performance of Gadolinia-Doped Ceria Diffusion Barrier Layers Fabricated by Pulsed Laser Deposition for Large-Area Solid Oxide Fuel Cells, ACS Appl. Energy Mater. 1 (2018) 1955-1964.

[21] D. Pérez-Coll, E. Céspedes, A.J. Dos Santos-García, G.C. Mather, C. Prieto, Electrical properties of nanometric CGO-thin films prepared by electron-beam physical vapour deposition, J. Mater. Chem. A 2 (2014) 7410-7420.

[22] M. Ismail, R. Ullah, R. Hussain, I. Talib, A. Manzoor Rana, M. Hussain, K. Mahmood, F. Hussain, E. Ahmed, D. Bao, Influence of argon and oxygen pressure ratio on bipolar-resistive switching characteristics of CeO_{2-x} thin films deposited at room temperature, Appl. Phys. A-Mater. 124 (2018) 89.

[23] S. Morlens, L. Ortega, B. Rousseau, S. Phok, J.L. Deschanvre, P. Chaudouet, P. Odier, Use of cerium ethylhexanoate solutions for preparation of CeO_2 buffer layers by spin coating, Mater. Sci. Eng. B 104 (2003) 185-191.

[24] T. Van Gestel, D. Sebold, H.P. Buchkremer, Processing of 8YSZ and CGO thin film electrolyte layers for intermediate- and low-temperature SOFCs, J. Eur. Ceram. Soc. 35 (2015) 1505-1515.

[25] B. Scherrer, J. Martynczuk, H. Galinski, J.G. Grolig, S. Binder, A. Bieberle-Hütter, J.L.M. Rupp, M. Prestat, L.J. Gauckler, Microstructures of YSZ and CGO thin films deposited by spray-pyrolysis: influence of processing parameters on the porosity, Adv. Funct. Mater. 22 (2012) 3509-3518.

[26] C.M. Halmenschlager, R.Neagu, L. Rose, C.F. Malfatti, C.P. Bergmann, Influence of the process parameters on the synthesis of gadolinium doped-ceria thin film, Mater. Res. Bull. 48 (2013) 207-213.

[27] D. Beckel, A. Bieberle-Hütter, A. Harvey, A. Infortuna, U.P. Muecke, M. Prestat, J.L.M. Rupp, L.J. Gauckler, Thin films for micro solid oxide fuel cells, J. Power Sources 173 (2007) 325-345.

[28] D. Marrero-López, R. Romero, F. Martín, J.R. Ramos-Barrado, Effect of the deposition temperature on the electrochemical properties of $La_{0.6}Sr_{0.4}Co_{0.8}Fe_{0.2}O_{3-\delta}$ cathode prepared by conventional spray-pyrolysis, J. Power Sources 255 (2014) 308-317.

[29] L. dos Santos-Gómez, E.R. Losilla, F. Martín, J.R. Ramos-Barrado, D. Marrero-López, Novel Microstructural Strategies To Enhance the Electrochemical Performance of $La_{0.8}Sr_{0.2}MnO_{3-\delta}$ Cathodes, ACS Appl. Mater. Interfaces 7 (2015) 7197-7205.

[30] L. dos Santos-Gómez, J.M. Porras-Vázquez, F. Martín, J.R. Ramos-Barrado, E.R. Losilla, D. Marrero-López, A novel multilaminated composite cathode for solid oxide fuel cells, Ceram. Inter. 45 (2019) 18124-18127.

[31] L. dos Santos-Gómez, J.M. Porras-Vázquez, E.R. Losilla, F. Martín, J.R. Ramos-Barrado, D. Marrero-López, LSCF-CGO nanocomposite cathodes deposited in a single step by spray-pyrolysis, J. Eur. Ceram. Soc. 38 (2018) 1647-1653.

[32] L. dos Santos-Gómez, J.M. Porras-Vázquez, E.R. Losilla, D. Marrero-López, Improving the efficiency of layered perovskite cathodes by microstructural optimization, J. Mater. Chem. A 5 (2017) 7896-7904.

[33] D. Marrero-López, M.C. Martín-Sedeño, J. Peña-Martínez, J.C. Ruíz-Morales, P. Núñez, J.R. Ramos-Barrado, Microstructure and conductivity of $La_{1-x}Sr_xGa_{0.8}Mg_{0.2}O_{3-\delta}$ electrolytes prepared using the freeze-drying method, J. Am. Ceram. Soc. 94 (2011) 1031-1039.

[34] Los Alamos National Lab, GSAS Program (1994) Rep. No. LA-UR-86748.

[35] X. Ke, S. Bals, A.R. Negreira, T. Hantschel, H. Bender, G. Van Tendeloo, TEM sample preparation by FIB for carbon nanotube interconnects, Ultramicroscopy 109 (2009) 1353-1359.

[36] J.C.C. Abrantes, Estereologia, Software Package ESTG/IPVC, Portugal, 2001.

[37] L.M. Acuña, J. Peña-Martínez, D. Marrero-López, R.O. Fuentes, P. Núñez, Electrochemical performance of nanostructured $La_{0.6}Sr_{0.4}CoO_{3-\delta}$ and $Sm_{0.5}Sr_{0.5}CoO_{3-\delta}$ cathodes for IT-SOFCs, J. Power Sources 196 (2011) 9276-9283.

[38] ZView: A Software Program for IES Analysis, Version 3.1, Scribner Associates, Inc., Southern Pines, NC, 2012.

[39] I. Miguel-García, S. Parres-Esclapez, D. Lozano-Castelló, A. Bueno-López, H_2 assisted decomposition of cerium nitrate to ceria with enhanced catalytic properties, Catal. Commun. 11 (2010) 848-852.

[40] S. Xue, W. Wu, X. Brian, Y. Wu, Dehydration, hydrolysis and oxidation of cerium chloride heptahydrate in air atmosphere, J. Rare Earth 35 (2017) 1156-1163.

[41] T. Arii, A. Kishi, M. Ogawa, Y. Sawada, Thermal decomposition of cerium(III) acetate hydrate by three-dimensional thermal analysis, Anal. Sci. 17 (2001) 875-880.

[42] U.P. Muecke, N. Luechinger, L. Schlagenhauf, L.J. Gauckler, Initial stages of deposition and film formation during spray pyrolysis – Nickel oxide, cerium gadolinium oxide and mixtures thereof, Thin Solid Films 517 (2009) 1522-1529.

[43] K.R. Lee, J.H. Lee, H.I. Yoo, Grain size effect on the electrical properties of nanocrystalline ceria, J. Eur. Ceram. Soc. 34 (2014) 2363-2370.

[44] J.G. Li, T. Ikegami, T. Mori, Low temperature processing of dense samarium-doped CeO_2 ceramics: sintering and grain growth behaviors, Acta Mater. 52 (2004) 2221-2228.

[45] J.L.M. Rupp, A. Infortuna, L.J. Gauckler, Microstrain and self-limited grain growth in nanocrystalline ceria ceramics, Acta Mater. 54 (2006) 1721-1730.

[46] R.B. Mos, T.Petrisor Jr., M. Nasui, A. Calleja, T. Puig, L. Ciontea,T. Petrisor, Enhanced structural and morphological properties of Gd-doped CeO_2 thin films obtained by polymer-assisted deposition, Mater. Lett. 124 (2014) 306-309.

[47] G. Chiodelli, L. Malavasi, V. Massarotti, P. Mustarelli, E. Quartarone, Synthesis and characterization of $Ce_{0.8}Gd_{0.2}O_{2-y}$ polycrystalline and thin film materials, Solid State Ionics 176 (2005) 1505-1512.

[48] N.I. Karageorgakis, A. Heel, T. Graule, L.J. Gauckler, Flame spray deposition of nanocrystalline dense $Ce_{0.8}Gd_{0.2}O_{2-\delta}$ thin films: Deposition mechanism and microstructural characterization, Solid State Ionics 192 (2011) 464-471.

[49] J. Tang, M.C. Hu, Z.H. Liu, C.S. Li, L.H. Jin, Epitaxial growth of solution derived $(Ce_{0.8}Gd_{0.2})_{1-x}Mn_xO_{2-\delta}$ films, Ceram. Int. 44 (2018) 14596-14600.

[50] M.G. Chourashiya, S.H. Pawar, L.D. Jadhav, Synthesis and characterization of $Gd_{0.1}Ce_{0.9}O_{1.95}$ thin films by spray pyrolysis technique, Appl. Surf. Sci. 254 (2008) 3431-3435.

[51] J.L.M. Rupp, A. Infortuna, L.J. Gauckler, Thermodynamic Stability of Gadolinia-Doped Ceria Thin Film Electrolytes for Micro-Solid Oxide Fuel Cells, J. Am. Ceram. Soc. 90 (2007) 1792-1797.

[52] B.B. Patil, S.H. Pawar, Structural, morphological and electrical properties of spray deposited nano-crystalline CeO_2 thin films, J. Alloys Compd. 509 (2011) 414-420.

[53] R. Martínez-Bautista, S.M. Fernández-Valverde, A. Tejada-Cruz, J.A. Chávez-Carvayar, Structural,morphological and electrical characterization of ceria-based nanostructured thin films obtained by ultrasonic spray pyrolysis, Bol. Soc. Esp. Ceram. V. 58 (2019) 38-47.

[54] S. Hong, H. Yang, Y. Lim, F.B. Prinz, Y.B. Kim, Grain-Controlled Gadolinia-Doped Ceria (GDC) Functional Layer for Interface Reaction Enhanced Low-Temperature Solid Oxide Fuel Cells, ACS Appl. Mater. Interfaces 11 (2019) 41338-41346.

[55] G. Balakrishnan, A.K. Panda, C.M. Raghvan, A. Singh, M.N. Prabhakar, E. Mohandas, P. Kuppusami, J. il Song, Microstructure, optical and dielectric properties of cerium oxide thin films prepared by pulsed laser deposition, J. Mater. Sci.: Mater. Electron. 30 (2019) 16548-16553.

[56] J.C.C. Abrantes, J.A. Labrincha, J.R. Frade, Applicability of the brick layer model to describe the grain boundary properties of strontium titanate ceramics, J. Eur. Ceram. Soc. 20 (2000) 1603-1609.

[57] J.T.S. Irvine, D.C. Sinclair, A.R. West, Electroceramics: characterization by impedance spectroscopy. Adv. Mater. 2 (1990) 132-138.

[58] C. Tian, S.W. Chan, Ionic conductivities, sintering temperatures and microstructures of bulk ceramic CeO_2 doped with Y_2O_3, Solid State Ionics 134 (2000) 89-102.

[59] R. Pereira Reolon, C. Melo Halmenschlager, R. Neagu, C. de Fraga Malfatti, C. Pérez Bergmann, Electrochemical performance of gadolinia-doped ceria (CGO) electrolyte thin films for ITSOFC deposited by spray pyrolysis, J. Power Sources 261 (2014) 348-355.

[60] G.F. Harrington, A. Cavallaro, D.W. McComb, S.J. Skinner, J.A. Kilner, The effects of lattice strain, dislocations, and microstructure on the transport properties of YSZ films, Phys. Chem. Chem. Phys. 19 (2017) 14319-14336.

[61] E. Perry Murray, M.J. Sever, S.A. Barnett, Electrochemical performance of $(La,Sr)(Co,Fe)O_3$–$(Ce,Gd)O_3$ composite cathodes, Solid State Ionics 148 (2002) 27-34.

[62] L. dos Santos-Gómez, J.M. Porras-Vázquez, E.R. Losilla, F. Martín, J.R. Ramos-Barrado, D. Marrero-López, Stability and performance of $La_{0.6}Sr_{0.4}Co_{0.2}Fe_{0.8}O_{3-\delta}$ nanostructured cathodes with $Ce_{0.8}Gd_{0.2}O_{1.9}$ surface coating, J. Power Sources 347 (2017) 178-185.

[63] G. Nurk k, M. Vestli, P. Möller, R. Jaaniso, M. Kodu, H. Mändar, T. Romann, R. Kanarbik, E. Lust, Mobility of Sr in Gadolinia Doped Ceria Barrier Layers Prepared Using Spray Pyrolysis, Pulsed Laser Deposition and Magnetron Sputtering Methods. J. Electrochem. Soc. 163 (2016) F88−F96.

[64] D. Szymczewska, J. Karczewski, A.Chrzan, P.Jasinsk CGO as a barrier layer between LSCF electrodes and YSZ electrolyte fabricated by spray pyrolysis for solid oxide fuel cells. Solid State Ionics 302 (2017) 113–117.

[65] T.T. Fister, D.D. Fong, J.A. Eastman, P.M. Baldo, M.J. Highland, P.H. Fuoss, K.R. Balasubramaniam, J.C. Meador, P.A. Salvador, In situ characterization of strontium surface segregation in epitaxial $La_{0.7}Sr_{0.3}MnO_3$ thin films as a function of oxygen partial pressure, Appl. Phys. Lett. 93 (2008) 151904-1−151904-3.